



# Compact adaptive-grid scheme for high numerical resolution simulations of isotachopheresis

Moran Bercovici<sup>a</sup>, Sanjiva K. Lele<sup>a,b</sup>, Juan G. Santiago<sup>b,\*</sup>

<sup>a</sup> Department of Aeronautics and Astronautics, Stanford University, Stanford, CA 94305, USA

<sup>b</sup> Department of Mechanical Engineering, Stanford University, Stanford, CA 94305, USA

## ARTICLE INFO

### Article history:

Received 17 July 2009

Received in revised form

23 November 2009

Accepted 24 November 2009

Available online 1 December 2009

### PACS:

47.61.–k

47.57.jd

87.15.Tt

87.50.ch

82.60.Hc

### Keywords:

Isotachopheresis

Electrophoresis

Displacement electrophoresis

Adaptive grid

Compact scheme

Chemical equilibrium

Electrokinetics

## ABSTRACT

In a previous publication we demonstrated a fast simulation tool for solution of electrophoretic focusing and separation. We here describe the novel mathematical model and numerical algorithms used to create this code. These include the representation of advection–diffusion equations on an adaptive grid, high-resolution discretization of the equations (sixth order compact), a new variational-based approach for controlling the motion of grid points, and new boundary conditions which enable solution in a moving frame of reference. We discuss the advantages of combining a high-resolution discretization with an adaptive grid in accurately resolving sharp interfaces in isotachopheresis, and provide verification against known analytical solutions and comparison with prevailing exiting numerical algorithms.

© 2009 Elsevier B.V. All rights reserved.

## 1. Introduction

Isotachopheresis (ITP) is an electrophoresis technique which allows for simultaneous separation and focusing of a wide range of chemical and biological species. The technique is useful in numerous applications including drug discovery, toxin detection, pharmacology, genetics and food analysis [1,2]. ITP is also very compatible with miniaturized chemical analysis systems as it is robust to implement, enhances sensitivity, and allows for separations in relatively short channels [3].

As shown schematically in Fig. 1, ITP uses a discontinuous buffer system consisting of leading (LE) and terminating electrolytes (TE). These respectively have higher and lower effective electrophoretic mobility than all other species in the system. Sample mixture is

introduced between the two (or can be included within the TE and/or LE). When an electric field is applied, all species separate simultaneously and focus into segregated zones according to their respective mobilities. Focusing occurs within an electric field gradient between the LE and TE as sample ions cannot overspeed the LE or underspeed the TE. ITP presents particularly difficult design and simulation challenges, as it typically results in extremely high gradients in both electric field and species concentration (e.g.,  $\sim 100$  mM concentration change over order  $1\ \mu\text{m}$  with a field gradient of  $10^4\ \text{V/m}^2$ ). This is due to non-linear electromigration physics which gives rise to ion concentration shock waves. Accurately resolving such sharp interfaces is of key importance in ITP as analytes often focus at these interfaces (e.g., analyte 2 in Fig. 1).

There has been significant advancement in recent years in the incorporation of additional physical modules into electrophoretic-transport solvers. For example, Mosher et al. added models for protein mobility [4] and electroosmotic flow [5]. Thormann et al. expanded the electroosmotic flow model to account for discontinuous buffer systems [6]. Hruska et al. [7] included the dependence of mobility and dissociation constant on ionic strength, and Bercovici

\* Corresponding author at: Department of Mechanical Engineering, Stanford University, 440 Escondido Mall, Bldg 530, Room 225, Stanford, CA 94305, USA. Tel.: +1 650 723 5689; fax: +1 650 723 7657.

E-mail address: [juan.santiago@stanford.edu](mailto:juan.santiago@stanford.edu) (J.G. Santiago).

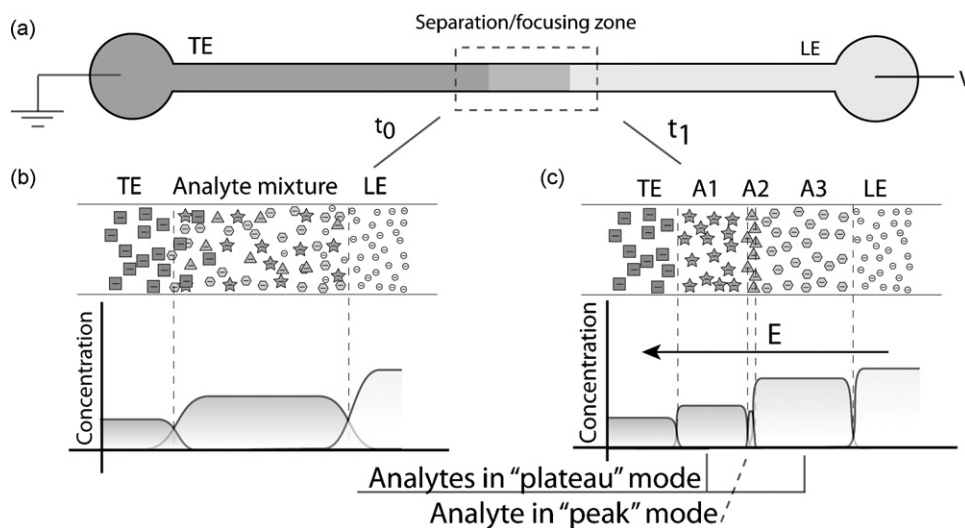


**Fig. 1.** Schematic of a typical finite-sample isotachopheresis process. (a) A simple microchannel is connected to two reservoirs. A mixed sample of analytes is introduced between a leading electrolyte (LE) and a trailing electrolyte (TE). (b) The interfaces between the various analytes are initially diffused, and analytes are mixed homogeneously. (c) An electric field is applied along the channel causing analytes to separate into distinct, focused zones. The interfaces between the various ion species sharpen, achieving a balance between electromigration and diffusion. Analytes (A1, A3) with initial relatively high concentration reach a “plateau mode” – in which concentration is saturated within a finite region of locally uniform concentration. Other analytes (A2) focus in “peak mode” and acquire an approximately Gaussian distribution whose width is determined by the interfaces of its neighboring electrolytes.

et al. [8] added a model for Taylor-type dispersion due to pressure-driven flow or non-uniform electroosmotic flow. An ideal solver is one capable of simulating essential physics (accounting for various and coupled phenomena), while providing numerically accurate results in a short time.

The problem of obtaining accurate, yet stable and non-oscillatory solutions for electrophoresis problems has engaged researchers for over 20 years. Existing proposed solutions can be roughly divided into non-dissipative centered schemes, requiring a large number of grid points to reduce oscillations, and to dissipative schemes offering faster solutions at the cost of physical accuracy. Dose and Guiochon [9] were perhaps the first to formally address the issue of numerical oscillations in the field of electrophoretic transport and derived a monotonicity condition for the case of a second order spatial discretization. This condition states that the cell Peclet number should satisfy throughout the domain  $Pe_{\Delta x} = a \Delta x / D < 2$ , where  $a$  is the advection velocity (the sum of electromigration and bulk flow in the case of ITP),  $D$  is the diffusion coefficient, and  $\Delta x$  is the grid spacing. For second order schemes on uniform grids, and at realistic electric fields and channel lengths, this requirement translates to  $O(10^3)$ – $O(10^4)$  grid points and to long computation times, sometimes on the order of days even on modern computers [10]. While such long computations may be satisfactory for basic research of electrophoretic transport phenomena, they can rarely serve as a design and optimization tool for experimentalists. While several new schemes have been proposed for dissipative solutions [11–15], non-dissipative implementations have essentially remained unchanged (from a numerical point of view) since the first implementation in 1983 [16], most utilizing a centered second order discretization on a uniform grid.

In [8], we reported an open-source simulation tool for one-dimensional electrophoresis, intended for use by the microfluidics community. We presented the various physical modules included in the code (including chemical equilibrium, electroosmotic flow, pressure-driven flow and dispersion) and compared its performance with existing standard techniques. We referred readers to a future publication for a detailed description of the numerical methods.

The current work provides full details and discussions, both theoretical and practical, for numerical simulations of ITP using

a high-order compact scheme coupled to an adaptive grid. While the numerical technique presented here is applicable to a wide range of electrophoretic application (and potentially to other one-dimensional non-linear advection–diffusion problems), we choose to focus here on ITP as it exhibits the most significant modeling challenges. In Section 2 we present the derivation of a new polynomial form for multi-species multi-valent chemical equilibrium which allows direct (rather than the typical iterative) solution of local pH. In modeling the governing equation we present the advection–diffusion equations entirely in terms of total concentration (as opposed to dependency on individual ionic states). This form is subsequently used in Section 3 to derive new characteristics based boundary conditions enabling solution in a moving frame of reference. In Section 3 we also derive the mapping of the equations from a non-uniformly gridded physical domain to a uniform-grid computational domain, and present our new variational approach technique for controlling the motion of grid points. Importantly, we provide in Sections 4 and 5 detailed verification of our numerical technique with emphasis on accuracy of interfaces, and study the numerical oscillations inherent to non-dissipative solutions as a function of the cell Peclet number. Throughout these sections, we provide comparison with prevailing existing numerical algorithms.

## 2. Governing equations

### 2.1. Equilibrium reactions

In many cases, accounting for chemical reactions, namely proton and hydroxyl dissociation, is important for accurate prediction of electromigration in general, and of isotachopheresis in particular. This is because mobility values for the majority of electrolytes are not constant; they depend on the dissociation level of the (weak) electrolyte which is a strong function of local pH values. In turn, since hydronium and hydroxide ions are shared by all reactions, pH values are a function of all chemical components in the system.

The use of equilibrium reaction has become fairly standard in the solution of electromigration problems and can be found in several publications including [4,17]. This is because electromigration and diffusion rates are typically much faster than the kinetic rates of the reactions, as originally shown in [17]. By combining the algebraic

equilibrium relations for all ionic states with the electroneutrality assumption, an implicit algebraic equation for the concentration of hydronium ions,  $c_H$ , can be derived. This equation is typically solved iteratively to obtain pH values in the channel. In this section we present the derivation of a new polynomial form for the equilibrium equation and discuss the construction of the polynomial coefficients. This polynomial form allows both for a direct solution of the equation, as well as a reduced cost in iterative solutions.

We begin with the net-neutrality equation expressed as a function of the total (analytical) concentrations  $c_i$ , the dissociation factor  $g_{i,z}$ , the hydronium concentration  $c_H$  and the water equilibrium coefficient  $K_W$ :

$$\sum_{i=1}^N c_i \sum_{z=n_i}^{p_i} z g_{i,z} + c_H - \frac{K_W}{c_H} = 0, \quad (1)$$

where  $(\cdot)_i$  indicates a property of the family  $i$ ,  $(\cdot)_{i,z}$  indicates a property of the ionic state  $z$  belonging to the family  $i$ , and  $n_i$  and  $p_i$  are respectively the minimum and maximum valence values within family  $i$ . A detailed derivation of Eq. (1) can be found in [18]. The dissociation factor is given by

$$g_{i,z} = \frac{L_{i,z} c_H^z}{\sum_{z=n_i}^{p_i} L_{i,z} c_H^z}, \quad (2)$$

where  $L_{i,z}$  are known constant coefficients obtained from the equilibrium coefficients of the different ionic states. Since the denominator in (1) is not a function of  $z$ , it can be removed from the inner summation to yield

$$c_H \sum_{i=1}^N \frac{c_i}{\sum_{z'=n_i}^{p_i} L_{i,z'} c_H^{z'}} \sum_{z=n_i}^{p_i} z L_{i,z} c_H^z + c_H^2 - K_W = 0. \quad (3)$$

By finding a common denominator to all three terms

$$c_H \sum_{i=1}^N c_i \left[ \prod_{\substack{j=1 \\ j \neq i}}^N \left( \sum_{z'=n_j}^{p_j} L_{j,z'} c_H^{z'} \right) \cdot \sum_{z=n_i}^{p_i} z L_{i,z} c_H^z \right] + \prod_{j=1}^N \left( \sum_{z'=n_j}^{p_j} L_{j,z'} c_H^{z'} \right) (c_H^2 - K_W) = 0. \quad (4)$$

Finally, merging the two terms under brackets, Eq. (4) can be written symbolically as

$$\sum_{i=1}^N c_i P_i + Q = 0, \quad (5)$$

where

$$Q = \prod_{j=0}^N Q_j, \quad P_i = c_H \prod_{j=1}^N \left( \sum_{z'=n_j}^{p_j} L_{i,z'} (1 + (z' - 1) \delta_{ij}) c_H^{z'-n_j} \right), \quad (6)$$

and

$$Q_0 = (c_H^2 - K_W), \quad Q_j = \prod_{z'=n_i}^{p_i} \left( \sum_{z'=n_i}^{p_i} L_{j,z'} c_H^{z'-n_j} \right).$$

While the expressions for  $P_i$  and  $Q$  may appear complex, they merely represent the coefficients of a polynomial, using the known quantities  $L_{i,z}$ . An important property of this new form of the net neutrality constraint is that the polynomials coefficients  $P_i$  and  $Q$  need to be calculated only for the first time step of the simulation, and these then hold for all spatial locations and subsequent times.

Only the concentrations  $c_i$  change in time and space, as described in the next section. As a result, only the summation over  $N$  species appearing in (5) has to be performed repeatedly. In addition, for the first step in the simulation (or for other problems where equilibrium needs to be solved just once) the roots of the polynomial can be computed directly by solving for the eigenvalues of the companion matrix. Furthermore, the polynomial form readily supplies the derivative of (5) without having to analytically or numerically derivate (1). This is convenient for implementation of iterative methods such as Newton–Raphson (for example, in subsequent time steps in the simulation, when the previous solution is a good initial condition), which make use of this derivative.

The polynomials  $Q$  and  $P_i$  are simple to construct using a matrix approach. For example, each of the polynomials  $Q_j$  can be considered to be the product of the matrix  $\hat{\mathbf{L}}$  and the vector  $\mathbf{c}_H$  consisting of powers of  $c_H$  from zero to  $r$ , where  $r$  is the highest possible power, given by  $r = \max_j (p_j - n_j)$ :

$$\begin{bmatrix} Q_0 \\ Q_1 \\ \vdots \\ Q_k \\ \vdots \\ Q_N \end{bmatrix} = \begin{bmatrix} -K_W & 0 & 1 & 0 & 0 \\ L_{1,n_1} & L_{1,n_1+1} & \dots & L_{1,p_1} & 0 \\ \vdots & \vdots & & \vdots & \vdots \\ L_{k,n_k} & \dots & L_{k,0} & \dots & L_{k,p_k} \\ \vdots & \vdots & \vdots & \vdots & \vdots \\ L_{N,n_N} & \dots & L_{N,p_N} & 0 & 0 \end{bmatrix} \begin{bmatrix} 1 \\ c_H \\ c_H^2 \\ c_H^3 \\ \vdots \\ c_H^{r-1} \\ c_H^r \end{bmatrix} = \hat{\mathbf{L}} \mathbf{c}_H. \quad (7)$$

In other words, row  $j$  in  $\mathbf{L}$  represents the coefficients of the corresponding polynomial  $Q_j$ . The rest of the row is padded with zeros to assure all lines have the same number of elements. To obtain  $Q$  we need to multiply all the polynomials  $Q_j$ . Alternatively, we can obtain the coefficients of  $Q$  by convolving all the rows of the matrix  $\hat{\mathbf{L}}$ . The polynomials  $P_i$  are constructed similarly.

## 2.2. Electromigration–diffusion equations

In [8] we employed a new form of the electromigration–diffusion equations which makes use of pH-dependent effective mobilities and diffusivities. This form was based on the approach taken by Saville and Palusinski [17,19], but is different in that the flux terms depend directly on the total concentrations instead of on individual ionic concentrations. In the **Supplementary Information** we show a simple derivation of this form, where the effective mobility and diffusivity naturally arise when the fundamental equations are expressed as a function of the dissociation factor  $g_{i,z}$ . Similar treatment is then given to the ionic flux, in order to determine the local electric field as a function of the current density and the total concentrations. This form proves useful in the derivation of characteristics boundary conditions as presented in Section 3.4.

The governing equation can be summarized with a set of advection–diffusion equations for the total concentrations  $c_i$ ,

$$\frac{\partial c_i}{\partial t} = \frac{\partial}{\partial x} \left[ \frac{\partial(D_i c_i)}{\partial x} + \mu_i \frac{\partial \phi}{\partial x} c_i - u c_i \right] \quad i = 1 \dots N, \quad (8)$$

and an equation for the electric field, obtained from invoking current conservation along the channel,

$$\frac{\partial \phi}{\partial x} = -\frac{1}{\sigma} \left( j + \frac{\partial S}{\partial x} \right). \quad (9)$$

Here  $\mu_i$  and  $D_i$  are respectively the effective mobility and diffusivity of the species family  $i$ , and are given by  $\mu_i = \sum_{z=n_i}^{p_i} \mu_{i,z} g_{i,z}(c_H)$  and

$D_i = \sum_{z=\eta_i}^{P_i} D_{i,z} \mathbf{g}_{i,z}(c_H)$ .  $u$  is an area-averaged bulk flow velocity,  $\sigma$  is the local conductivity, and  $\partial S/\partial x$  is a term associated with diffusive current. All terms are fully described in detail in the [Supplementary Information](#).

### 3. Numerical method

We take a non-dissipative approach in the solution of the equations to allow accurate resolution of ITP interfaces. As mentioned earlier, the typically cited [9] condition for guiding the discretization (or grid spacing) of the domain is that the cell Peclet number satisfy

$$Pe_{\Delta x} = \frac{a \Delta x}{D} < 2. \quad (10)$$

However, this approach is over-restricting as it gives no consideration to the range of wave numbers appearing in the problem. Oscillations, if they appear, are the result of unresolved wave numbers exhibiting dispersion. For a smooth functions (as is the case for all solution discussed in this work), such unresolved wave numbers would appear in regions of high gradients where the spatial resolution of the discretization is insufficient. Thus, as long as regions of high gradients satisfy this requirement (or its equivalent for other schemes), regions of low gradients can be more sparsely gridded, and yet maintain a non-oscillatory solution. Furthermore, *a priori* choice of the grid spacing according to (10) is often non-trivial as the advection velocity is space, time, and species dependent.

To address these issues, the numerical approach we propose is composed of two main components. The first is the use of a sixth order compact scheme which offers higher resolution and thus decreases the number of grid points required to accurately capture sharp gradients. The second is the development of an adaptive grid procedure which is able to dynamically concentrate grid points at regions of high gradients at the expense of regions with shallower gradients. While this approach does not mathematically guarantee monotonicity, we are able to achieve smooth and stable results at high electric fields, while decreasing the computational time by nearly two orders of magnitude. In Section 3.1 we formulate the governing equations on a non-uniform grid, by mapping the physical domain onto a uniform computational domain. In Section 3.2 we present our variational approach for dynamically adapting the grid mapping based on local gradients in the solution. In Section 3.3 we present the spatial discretization scheme, and finally in Section 3.4 develop the boundary conditions.

#### 3.1. Transformation from physical to computational domain

Taking the approach offered by Spatz and Carey [20], we define a mapping function between the physical domain  $x$ , having a non-uniform grid, and the computational domain  $z$ , having a uniform grid. Considering the mapping function to be of the form  $x=x(z)$ , the first derivative with respect to  $x$  can be expressed in terms of  $z$  as

$$\frac{\partial(\cdot)}{\partial x} = \frac{\partial(\cdot)}{\partial z} \frac{\partial z}{\partial x} = \frac{1}{x_z} \frac{\partial(\cdot)}{\partial z}, \quad (11)$$

where  $x_z$  denotes a derivative of  $x$  with respect to  $z$ . Similarly, the second derivative is given by

$$\frac{\partial^2(\cdot)}{\partial x^2} = \frac{1}{x_z^2} \frac{\partial^2(\cdot)}{\partial z^2} - \frac{\partial(\cdot)}{\partial z} \frac{x_{zz}}{x_z^3}. \quad (12)$$

In addition, the partial time derivative takes the form

$$\frac{\partial(\cdot)}{\partial t} \Big|_{x=\text{const}} = \frac{\partial(\cdot)}{\partial t} \Big|_{z=\text{const}} - \frac{\partial(\cdot)}{\partial x} \frac{\partial x}{\partial t} = \frac{\partial(\cdot)}{\partial t} \Big|_{z=\text{const}} - \frac{\partial(\cdot)}{\partial z} \frac{1}{x_z} \frac{\partial x}{\partial t}. \quad (13)$$

Substituting Eqs. (11)–(13) into (8) and (9), we obtain the advection–diffusion equation in the computational domain

$$\begin{aligned} \frac{\partial c_i}{\partial t} = & \frac{1}{x_z^2} \left[ \frac{\partial^2(c_i D_i)}{\partial z^2} - \frac{\partial(c_i D_i)}{\partial z} \frac{x_{zz}}{x_z} \right. \\ & \left. + \mu_i c_i \left( \frac{\partial^2 \phi}{\partial z^2} - \frac{x_{zz}}{x_z} \frac{\partial \phi}{\partial z} \right) + \frac{\partial(\mu_i c_i)}{\partial z} \frac{\partial \phi}{\partial z} \right] + (x_t - u) \frac{\partial c_i}{\partial z} \frac{1}{x_z}, \end{aligned} \quad (14)$$

with

$$\frac{\partial \phi}{\partial z} = -\frac{1}{\sigma} \left( j x_z + \frac{\partial S}{\partial z} \right), \quad (15)$$

and

$$\left( \frac{\partial^2 \phi}{\partial z^2} - \frac{x_{zz}}{x_z} \frac{\partial \phi}{\partial z} \right) = -\frac{1}{\sigma} \left( \frac{\partial^2 S}{\partial z^2} - \frac{\partial S}{\partial z} \frac{x_{zz}}{x_z} + \frac{\partial \sigma}{\partial z} \frac{\partial \phi}{\partial z} \right). \quad (16)$$

Eq. (14) can now be discretized using standard uniform grid schemes. It remains to determine the mapping function  $x(z)$  at all times. This is done using an adaptive meshing procedure described in Section 3.2.

#### 3.2. Adaptive mapping

We wish to increase the grid density in areas of high gradients in the solution, at the expense of low gradient regions. To obtain this type of grid distribution, we minimize the following cost function

$$\begin{aligned} J[x] = & \int_0^L w(z) \left( \frac{\partial x}{\partial z} \right) dx = \int_0^L w(z) \frac{\partial x}{\partial z} \left( \frac{\partial x}{\partial z} dz \right) \\ = & \int_0^L w(z) x_z^2 dz, \end{aligned} \quad (17)$$

where  $w(z)$  will be referred to as the regulating function. As the functional is minimized, regions where the regulating function acquires high values will result in small  $x_z$  values (higher grid density). To minimize the functional, let us look at the variation

$$\begin{aligned} \delta J = & J[x + \delta x] - J[x] = \int_0^L w(z) \left( \frac{\partial x}{\partial z} + \frac{\partial \delta x}{\partial z} \right)^2 dz \\ & - \int_0^L w(z) \left( \frac{\partial x}{\partial z} \right)^2 dz. \end{aligned} \quad (18)$$

Omitting non-linear terms, we obtain

$$\delta J = 2 \int_0^L w(z) \frac{\partial x}{\partial z} \frac{\partial \delta x}{\partial z} dz. \quad (19)$$

Since the length of the physical domain is fixed, no perturbations are allowed at its end point, i.e.,  $\delta x|_0 = \delta x|_L = 0$ . Integrating by parts yields

$$\delta J = 2 \int_0^L \frac{\partial}{\partial z} \left( w(z) \frac{\partial x}{\partial z} \right) \delta x dz. \quad (20)$$

The functional is minimized when  $\delta J = 0$ , which leads to the requirement that the integrand must vanish,

$$\frac{\partial}{\partial z} (w x_z) = 0. \quad (21)$$

Directly solving for  $x(z)$  from (21) will require the solution of an ODE at each time step and interpolation of the solution on the new grid. Instead, we may try and approach the minimum by stepping

in the right direction to minimize  $\delta J$ , as proposed by Jameson et al. [21]. Specifically, if we choose

$$\delta x = -\lambda \frac{\partial}{\partial z}(wx_z), \quad (22)$$

where  $\lambda$  is some positive scalar, (20) becomes

$$\delta J = -\lambda \int_0^L \left[ \frac{\partial}{\partial z}(wx_z) \right]^2 dz. \quad (23)$$

Since  $J \geq 0$  and  $\delta J \leq 0$ , adoption of relation (22) will always result in incremental steps taken towards the optimum. We may regard Eq. (22) as an additional, coupled hyperbolic equation, describing the motion of grid points in the physical domain,

$$\frac{\partial x}{\partial t} = -\lambda \frac{\partial}{\partial z}(wx_z) \triangleq -\lambda g(z). \quad (24)$$

However,  $g(z)$  involves two derivatives with respect to  $z$ , hence at each time step  $x$  becomes less smooth by two classes. To solve this problem, Jameson et al. [21] suggested the following smoothing operator

$$\bar{g} - \varepsilon \frac{d^2 \bar{g}}{dz^2} = g, \quad (25)$$

where  $\bar{g}$  is the modified gradient, and  $\varepsilon$  is a smoothing parameter. As  $\varepsilon \rightarrow 0$   $\bar{g} \rightarrow g$ , and as  $\varepsilon \rightarrow \infty$   $\bar{g} \rightarrow 0$ . The final equation for the adaptive grid is hence

$$\frac{\partial x}{\partial t} = -\lambda \bar{g}(z). \quad (26)$$

It remains to determine the regulating function  $w(z)$  that will drive the adaptive grid. Since we are interested in increasing grid density in regions of high gradients, a natural choice would be

$$\mathbf{w}_i^{***} = \left| \frac{\partial c_i}{\partial z} \right| \quad i = 1 \dots N, \quad (27)$$

where  $i$  indicates a specific species. The weight function of each species is then normalized by its maximum value in the domain, to yield a set of vectors (one for each species) which are all of order unity,

$$\mathbf{w}_i^{**} = \frac{\mathbf{w}_i^{***}}{\max(\mathbf{w}_i^{***})}. \quad (28)$$

At each grid point the maximum value of all species is chosen

$$\mathbf{w}^* = \max(\mathbf{w}_i^{**}). \quad (29)$$

A constant is added to force equidistribution when the regulating function is uniformly zero,

$$\mathbf{w} = K_{AG} + \mathbf{w}^*. \quad (30)$$

Two parameters remain to be determined by the user:  $\lambda$  and  $K_{AG}$ .  $\lambda$  can be regarded as the speed at which the grid adapts to changes in the regulating function. If its chosen value is too small, the grid will not adapt fast enough to gradients forming in the channel. On the other hand, since (24) is propagated together with the governing equation, if its value is too high, it may limit the stable time step. Numerical experimentation shows that a value of  $\lambda = 1$  works well for most ITP applications. The parameter  $K_{AG}$  determines the relative weight assigned to regions of zero gradients, and thus strongly affects the overall grid distribution. Lower values of  $K_{AG}$  tend to deplete zero-gradient regions of grid points, focusing them at sharp interface. Higher values of  $K_{AG}$  result in a nearly static (uniform) grid distribution with little or no grid enrichment at sharp interfaces. In the [Supplementary Information](#) we present a guideline for the choice of  $K_{AG}$ , based on a simple scaling analysis of the steady state grid distribution. We show that the parameter  $K_{AG}$  can be expressed as a function of the number of grid points

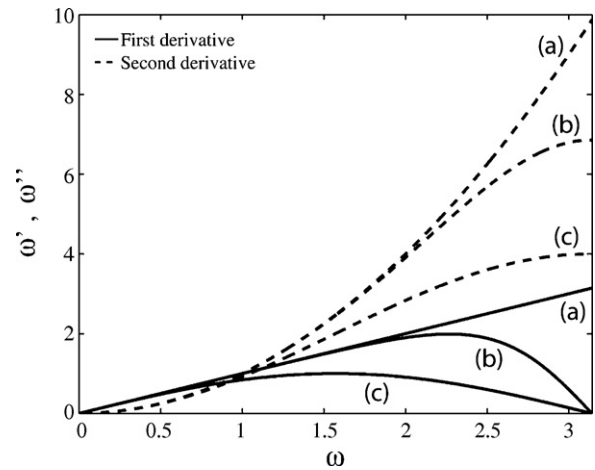


**Fig. 2.** Modified wave number due to numerical discretization versus true wave number, for first and second derivative approximations ( $w'$  and  $w''$  respectively). (a) Exact differentiation, (b) sixth order compact scheme – Eqs. (31) and (33), and (c) second order central differences scheme. The sixth order compact scheme is able to accurately resolve higher wavelengths, thus exhibiting higher resolution compared with the second order central differences scheme.

$N_I$  that one wishes to place at each ITP interface. This allows the use of a single parameter value across different simulations (e.g., at different current densities).

### 3.3. Spatial discretization

The choice of spatial discretization is key for the accurate resolution of sharp interfaces. In [8] we showed that the use of numerical dissipation leads to overly diffused interfaces and thus fails to accurately predict the concentration distribution of analytes focused at those interfaces. A centered scheme is therefore a natural choice for the spatial discretization. However, monotonicity of the solution is not guaranteed, and the possibility and occurrence of spurious oscillations is largely dependent on the ability of the scheme to resolve high wave numbers. A significant number of studies have been published in the field of electrophoretic transport which dealt with the reduction or elimination of such oscillations [11,13–15]. However, the majority of solutions proposed involved some form of numerical dissipation. Centered schemes, when used, were always limited to second order.

Higher resolution can be readily obtained by employing a centered compact scheme, as suggested by Lele [22]. Here, we chose a sixth order compact scheme which offers significantly higher resolution compared to an explicit second order scheme, at the cost of solving a tridiagonal system. Fig. 2 compares the first and second derivative resolution of both schemes. Examining the first derivative, the standard second order centered scheme resolves 25%, 8% and 2% of the wave numbers to an accuracy of 10%, 1% and 0.1% respectively. This is compared to the sixth order compact scheme with resolving efficiencies of 70%, 50% and 35% for the same accuracies. The scheme uses a five point symmetric stencil for all internal grid points. The approximation for the first derivative is given by

$$\frac{1}{3}f'_{j-1} + f'_j + \frac{1}{3}f'_{j+1} = \frac{1}{\Delta z} \left[ \frac{1}{9} \frac{f_{j+2} - f_{j-2}}{4} + \frac{14}{9} \frac{f_{j+1} - f_{j-1}}{2} \right]. \quad (31)$$

Since ITP boundary conditions are non-periodic, a fifth order skewed scheme is used at two nodes at each boundary. For the

left boundary for example,

$$f_1' + 4f_2' = \frac{1}{\Delta z} \left[ -\frac{37}{12}f_1 + \frac{2}{3}f_2 + 3f_3 - \frac{2}{3}f_4 + \frac{1}{12}f_5 \right],$$

and

$$\frac{1}{6}f_1'' + f_2'' + \frac{1}{2}f_3'' = \frac{1}{\Delta z} \left[ -\frac{10}{18}f_1 - \frac{1}{2}f_2 + f_3 + \frac{1}{18}f_4 \right].$$

Similarly, the internal-points approximation for the second derivative is given by

$$\frac{2}{11}f_{j-1}'' + f_j'' + \frac{2}{11}f_{j+1}'' = \frac{1}{\Delta z^2} \left[ \frac{3}{11} \frac{f_{j+2} - 2f_j + f_{j-2}}{4} + \frac{12}{11} \frac{f_{j+1} - 2f_j + f_{j-1}}{1} \right],$$

and at the boundaries,

$$f_1'' + \frac{137}{13}f_2'' = \frac{1}{\Delta z^2} \left[ \frac{1955}{156}f_1 - \frac{4057}{156}f_2 + \frac{1117}{78}f_3 - \frac{55}{78}f_4 - \frac{29}{156}f_5 + \frac{7}{156}f_6 \right]$$

$$\frac{1}{10}f_1'' + f_2'' - \frac{7}{20}f_3'' = \frac{1}{\Delta z^2} \left[ \frac{99}{80}f_1 - 3f_2 + \frac{93}{40}f_3 - \frac{3}{5}f_4 - \frac{3}{80}f_5 \right].$$

Eqs. (31)–(34) constitute two closed systems. The solution of these systems yields approximations to the first and second derivative at all grid points in the computational domain. The derivatives are then used in Eq. (14) to obtain the local time derivative at every point. It is important to note that by using (32) and (34), the boundary values are modified according to information obtained from within the domain. This boundary condition is of course not generally true; in many physical cases the boundary conditions are fixed, or information propagates from the outside. For example, in typical isotachopheresis problems wherein the solution domain consist of a microchannel (or capillary) between end-channel reservoirs. In Section 3.4 we detail another step in the solution where the time derivatives at the boundaries are determined according to the direction of the local characteristics.

In order to maintain an overall sixth order accuracy, we also discretized the grid mapping  $x=x(z)$  using the same sixth order compact scheme: At each time step, we compute the new grid point coordinates according to (26). We then compute new values for  $x_z$  and  $x_{zz}$  using the sixth order operators (31)–(34). These derivatives are then used in the next time step in the governing equations (14)–(16), as well as in the new calculation of the cost function (23). The smoothing operator (25), however, need not be discretized with the same accuracy, as a smoothed gradient  $\bar{g}$  of lower accuracy impacts only the absolute values of the grid points. The accuracy of governing equations are unaffected by the smoothing procedure, provided that the derivatives  $x_z$  and  $x_{zz}$  are computed to a sufficiently high accuracy. We therefore discretized Eq. (25) using standard second order central differences.

### 3.4. Boundary conditions

Published discussions (and analyses) of boundary conditions for electrophoretic transport problems are very limited. For example, Palusinski et al. [19] and Dose and Guiochon [9] used strictly fixed concentration values at the boundaries; while Sounart and Baygents [11], Ikuta and Hirokawa [14], Ermakov et al. [12], and Hruska et al. [7] did not explicitly discuss the boundary conditions. One notable exception is Breadmore et al. [10], who recently extended their code (based on the code by Palusinski et al.) to allow extrapolation from the domain onto the boundary, thus allowing waves to leave the domain.

Many ITP simulations are possible using long domains at which the ITP interfaces are at all times far from the boundaries and concentration values are fixed at both ends. However, there is an obvious advantage in computational time to employing smaller domains in the region of interfaces and ITP zones of interest. In our

experience, there is much benefit also in analyzing a frame of reference moving with the interface(s) of interest. In such cases, as the TE and analytes assume new concentration values (according to the Kohlrausch regulating function [23] for fully ionized ions, or, more generally, the Jovin [24] and Alberty [25] relations), concentration waves are sent from the interface and towards the boundaries. For such cases, a code should properly allow these waves to leave the domain and avoid non-physical reflections.

First we determine the direction of waves at the boundaries. For waves leaving the domain, the boundary value will be determined by solving the equation using backward differences, as described in Section 3.3. For waves entering the domain, the boundary conditions will be fixed according the concentration in the reservoir. If the reservoir concentration is constant in time, the latter is equivalent to setting the time derivative at the boundary to zero.

Note that the direction of wave propagation cannot be determined solely by the sign of the velocity for each species (such an approach were employed, for example, in the explicit upwinding schemes used by Ikuta and Hirokawa [14] and Sounart and Baygents [11]). We first explore the reason for this complexity, and then present a more general method.

The complexity of these boundary conditions can be explained by analyzing a simple advection and electromigration problem. Neglecting diffusion for the moment, we can write the flux,  $f$ , of some species  $i$  as

$$f_i = (\mu_i E - u)c_i, \quad (35)$$

where  $E$  is the electric field. By inspection, and by analogy to linear PDEs, one might conclude that the wave velocity is given by the coefficient of  $c_i$ ,  $\mu_i E - u$ , and therefore that the sign of this quantity determines the direction of wave propagation. However, the electric field is also coupled to the concentration  $c_i$  (and to all other concentrations in the system, e.g., by net neutrality) and so

$$\frac{df_i}{dc_i} = (\mu_i E - u) + \mu_i c_i \frac{\partial E}{\partial c_i}. \quad (36)$$

The electric field can be expressed as the ratio of current density to conductivity,  $E=j/\sigma$ , and (36) becomes

$$\frac{df_i}{dc_i} = (\mu_i E - u) - \frac{\mu_i c_i j \alpha_i}{\sigma^2} = \mu_i E \left( 1 - \frac{\alpha_i c_i}{\sigma} \right) - u, \quad (37)$$

where  $\alpha_i$  is defined as  $\sum_{z=\eta_1}^{p_i} g_{i,z} \mu_{i,z} F$  (see [Supplementary Information document](#)), and  $\alpha_i c_i$  is the conductivity of the species  $i$ . Clearly, when the relative conductivity of the species of interest is low,  $0 < \alpha_i c_i / \sigma \ll 1$ , the wave direction and the direction of ion migration (velocity) are equal. However, as the relative conductivity increases, the sign of the expression on the right-hand side of (37) may change. This change of sign results in a species which can have a velocity vector pointing in the direction of electromigration, while its concentration gradients propagates in the opposite direction. Although the latter example is an over-simplification, it serves to highlight the importance of wave propagation analyses. In short, the complexity of the problem arises from the dependency of the electric field on all species in the system (and electroneutrality insures a coupling between ions and counter-ions).

Moore [26] presented an analytical study of ITP where he provided a characteristic representation of the (hyperbolic) governing equations. We here use characteristics theory to obtain a more rigorous analysis of the wave direction, leading to a new set of boundary conditions. To achieve this, we seek to express the system of (coupled) transport equation in a semi-linear form of the type  $\partial \mathbf{c} / \partial t = \mathbf{A} \partial \mathbf{c} / \partial x$ , where  $\mathbf{c}$  is the vector of species concentrations  $c_i$  and  $\mathbf{A}$  is a matrix of (generally non constant) coefficients. This process becomes more complex when equilibrium chemistry is involved since all species concentrations and their properties (such as effective mobility) are coupled through the algebraic constraint

(5). In order to overcome this complexity, we make use of three simplifying assumption: First, we assume safe pH conditions (i.e., that the concentration of the migrating species of interest are significantly larger than the concentrations of hydronium and hydroxide ions) at the boundaries. This allows excluding the explicit dependence of conductivity on hydronium and hydroxide concentration. Second, we assume the system is well buffered (i.e., that the sensitivity of all variables to slight changes in pH is small) at the boundaries. This allows treating species' pH-dependent properties (e.g., effective mobility) as locally constant. Third, we assume current is carried mostly by electromigration (versus diffusion). This allows expressing the electric field as a function of the conductivity and the (known and constant) current density,

$$\frac{\partial \phi}{\partial x} \simeq -\frac{\eta}{\sigma}, \quad (38)$$

While the assumptions presented here do not necessarily hold for any electrophoretic transport problem, they are useful for a wide range of real ITP applications. In particular, these assumptions are useful for the solution of ITP problems in a frame of reference moving with the interface(s). In this case, the sharp gradients are always contained within the domain, while low-gradient adaptation waves propagate out of the domain. For ITP problems solved in the frame of reference of the lab (ITP interfaces are moving), these assumptions would generally hold as long as the sharp ITP interfaces remain far from the boundaries.

Using the first assumption, of safe pH at the boundaries, the gradient of the electric field can be expressed as

$$\frac{\partial^2 \phi}{\partial x^2} = \frac{\eta}{\sigma^2} \sum_{j=1}^N \frac{\partial \sigma}{\partial c_j} \frac{\partial c_j}{\partial x} = \frac{\eta}{\sigma^2} \sum_{j=1}^N \alpha_j \frac{\partial c_j}{\partial x}. \quad (39)$$

Note that the explicit dependency of the conductivity on  $c_H$  and  $c_{OH}$  does not appear in this expression. However, the different  $\alpha_j$  remain a function of pH and express the dependency of the conductivity on the dissociation factor of each species family. Using (39), the hyperbolic part of (8) can be written as

$$\frac{\partial c_i}{\partial t} = \mu_i c_i \frac{\eta}{\sigma^2} \sum_{j=1}^N \alpha_j \frac{\partial c_j}{\partial x} + \left( \mu_i \frac{\partial \phi}{\partial x} - u \right) \frac{\partial c_i}{\partial x}. \quad (40)$$

Evaluated at the boundary, the last expression can be written in matrix form as

$$\frac{\partial \mathbf{c}}{\partial t} = \mathbf{A} \frac{\partial \mathbf{c}}{\partial x} = (\mathbf{A}_1 + \mathbf{A}_2) \frac{\partial \mathbf{c}}{\partial x}, \quad (41)$$

where the matrices  $\mathbf{A}_1$  and  $\mathbf{A}_2$  are given by

$$\begin{aligned} \mathbf{A}_1 &= \text{diag}(\mathbf{p}) \\ \mathbf{A}_2 &= \mathbf{q}^T \mathbf{r} \end{aligned}, \quad (42)$$

and

$$\mathbf{p}_i = \mu_i \frac{\partial \phi}{\partial x} - u, \quad \mathbf{q}_i = \frac{\eta}{\sigma^2} c_i \mu_i, \quad \mathbf{r}_i = \alpha_i. \quad (43)$$

At each time step, the time derivatives at both boundaries are then converted to the characteristic variables by calculating the eigenvalues and eigenvectors of the matrix  $\mathbf{A}$ ,

$$\frac{\partial \mathbf{R}}{\partial t} = \mathbf{V}^{-1} \frac{\partial \mathbf{c}}{\partial t}. \quad (44)$$

Here  $\mathbf{V}$  is matrix whose rows are the eigenvectors of  $\mathbf{A}$ . In the characteristics space, the direction of the characteristics is identifies by the sign of their eigenvalues. For the characteristics propagating into the domain, the time derivative information from within the

domain is invalid, and their time derivatives are set to zero. For the left boundary for example,

$$\frac{\partial R_i^*}{\partial t} = \begin{cases} \frac{\partial R_i}{\partial t} & \lambda_i \geq 0 \\ 0 & \lambda_i < 0 \end{cases}. \quad (45)$$

The characteristic variables are then converted back to the primitive variables,

$$\frac{\partial \mathbf{c}}{\partial t} = \mathbf{V} \frac{\partial \mathbf{R}^*}{\partial t}, \quad (46)$$

to yield the time derivative that will be used at the boundary.

Eq. (46) expresses the change in concentration at the boundaries only due to information propagating from within the domain and towards the boundary. The information from waves that are propagating into the domain is excluded and prevented from being extrapolated onto the boundary. While several strict assumptions are required to obtain this result, these assumptions hold for many realistic problems of interest. An example solution for a case of analyte focusing using ITP, solved in a frame of reference moving with the plug, is presented in Section 5. For cases where the system is either poorly buffered or outside of safe pH, we resort to using significantly longer computational domains such that significant wave fronts do not reach the boundaries within the computational time of interest. The adaptive grid procedure is useful in such cases, as little computational cost is spent on long regions of the domain where the solution exhibits concentration plateaus.

### 3.5. Time discretization

Capturing the transient dynamics of electrokinetics is key to the design of injection schemes, detector placement, and prediction of stacking and focusing rates and analyte concentration [27,28]. To enable operation across different initial conditions and buffer systems and yet avoid waste in computational time, we make use of the third order Runge–Kutta–Bogacki–Shampine (RK23) scheme. This method uses two sequential Runge–Kutta orders to estimate truncation error, and adjusts the time step accordingly. For completeness, the Runge–Kutta steps and the error estimation are provided in the [Supplementary Information](#).

## 4. Verification

The results presented here were obtained using an un-compiled version of the code under Matlab release version R2007b on a 32 bit Windows XP operating system. An Intel Core 2 Duo 2.0 GHz T7300 CPU with 2 GB of RAM was used as the computing platform (using only one of the cores).

### 4.1. Plateau values

For zones achieving plateau mode under ITP, a semi-analytical (iterative) solution exists for the concentration values as a function of their chemical properties and the properties of the LE and counter-ion [29]. Comparison of the simulation with these analytical values allows verification of the implementation of the chemical equilibrium physics, the conductivity and electric field calculations, and the modified fluxes due to the adaptive grid. Fig. 3 presents the separation and focusing of five acids (both strong and weak) achieving plateau values. The names and properties of the different species (including the LE, TE and counter-ion) are listed in Table 1a. The species were chosen so to represent strong acids (LE, A2), monovalent weak acids (A3, A5, TE), polyvalent weak acids (A1) and ampholytes (A4). Table 1b presents a comparison between simulation and analytical results for pH values, concentration, and

**Table 1**

Quantitative verification of plateau value calculations. (a) List of valence,  $pK_a$ , and mobility values used in the simulation. (b) Comparison of analytical (shaded columns, italicized font) and numerical (white columns, Roman font) values obtained for pH, concentration, and effective mobility in plateau mode ITP.

(a) Figure symbol	Acid name	Valence	$pK_a$	$\mu_{zi} (\times 10^9 \text{ m}^2/\text{Vs})$
LE	Hydrochloric	-1	-2	-79.1
A1	Arsenic	-1	2.19	-35.2
		-2	6.94	-70
A2	Sulfamic	-1	-2	-50.3
A3	Acetic	-1	4.756	-42.4
A4	Aspartic	+1	1.99	+31.6
		-1	3.9	-31.6
		-2	10.002	-51.8
A5	Cacodylic	-1	6.184	-29.9
TE	3-Phenylpropionic	-1	4.664	-26.5

(b) Figure symbol	Acid name	pH	$c$ (mM)	$\mu_i (\times 10^9 \text{ m}^2/\text{Vs})$
LE	Hydrochloric	7.77	100.0	-79.1
A1	Arsenic	7.83	49.4	-66.4
A2	Sulfamic	7.84	86.5	-50.3
A3	Acetic	7.87	81.0	-42.4
A4	Aspartic	7.93	70.4	-31.9
A5	Cacodylic	7.95	69.1	-29.4
TE	3-Phenylpropionic	7.96	65.0	-26.5

□: Numerical; ■: analytical.

effective mobility in each region. For most species and properties presented, results agree to three significant digits. For arsenic acid and aspartic acid, results agree to two significant digits (0.6% difference).

#### 4.2. Interface shape

Palusinski et al. [30] studied the effect of the net-neutrality approximation on the shape of an ITP interface, and concluded it can be safely used for typical ITP conditions. Saville and Palusinski [17] and earlier MacInnes and Longworth [31] used this approximation to provide a simple analytical solution for the width of an ITP interface. The solution describes a three species ITP problem, consisting of two co-ions and a single counter-ion. While a closed-form solution for the concentrations could not be obtained, their analysis provided an explicit expression for the ratio of LE to TE

concentrations as follows:

$$\frac{c_{LE}}{c_{TE}} = e^{-x/\delta}, \quad (47)$$

where  $x$  is the spatial coordinate, and  $\delta$  is the characteristic width of the interface given by

$$\delta = R_{\mu} T z_{LE} \left( \frac{\mu_{TE}(\mu_{LE} - \mu_{Cl})}{\mu_{LE} - \mu_{TE}} \right) \frac{c_{LE}^0}{j}. \quad (48)$$

Subscripts  $TE$ ,  $LE$  and  $Cl$  indicate properties related to the trailing electrolyte, leading electrolyte, and counter-ion respectively.  $c_{LE}^0$  is the plateau value of the leading electrolyte.

We here use this analytical result as a basis for comparison in testing the accuracy of our numerical scheme. To obtain numerical results to compare with the analytical formula, we deactivated our chemistry module to produce idealized simulations wherein no other species exist in the system (no hydronium or hydroxide ions). A single ITP interface was simulated using fully ionized LE, TE and counter-ion having mobilities of  $-8 \times 10^{-8}$ ,  $-2 \times 10^{-8}$  and  $+5 \times 10^{-8} \text{ m}^2 \text{ V}^{-1} \text{ s}^{-1}$  respectively. The problem was solved in a frame of reference moving with the LE, so that the interface appears stationary and a steady state solution can be obtained. The LE concentration was set to 100 mM, and an equal concentration was set for the counter-ion to satisfy electroneutrality. The domain was 10 mm long and discretized using 100 grid points. The interface shape was simulated for current value of 0.1, 1 and 5  $\mu\text{A}$ , and current densities consistent with a 90  $\mu\text{m}$  wide, 20  $\mu\text{m}$  deep D-shaped channel.

Fig. 4a presents the concentration profiles obtained from solutions of the 1  $\mu\text{A}$  case using various spatial discretization schemes. The results are presented on a non-dimensional scale where the concentration has been normalized by  $c_{LE}$  and the axial coordinate has been normalized by the characteristic length  $R_{\mu} T \mu_{LE} z_{LE} c_{LE} / j$ . Fig. 4b presents on a logarithmic scale the ratio of LE to TE concentrations versus the normalized axial coordinate. The analytical result (47) appears as a solid line. The first order upwind scheme results in a significantly diffused interface, even when upwinding is coupled to the adaptive-grid scheme. This is expressed as a significant deviation from the linear analytical solution, for all spatial locations. The second order centered scheme (with adaptive grid), being non-dissipative in nature, performs significantly better and is able to capture the correct slope, at least close the origin.

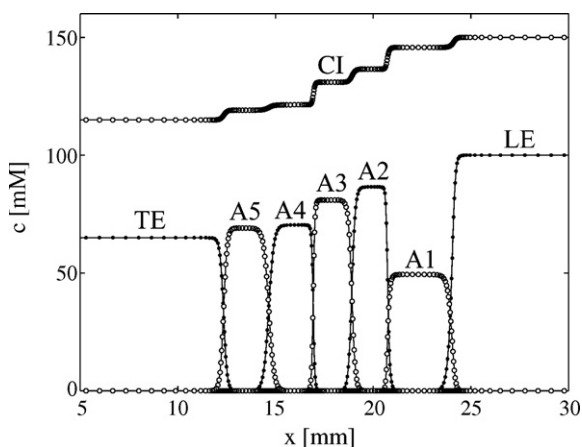


**Fig. 3.** Concentration profiles for plateau mode ITP focusing and separation of five strong and weak acids. Dots and circles on curves indicate the location of grid points (both symbols are used and alternated for clarity of presentation). The simulation was performed using 200 grid points on a 40 mm long channel. A constant current of 2  $\mu\text{A}$  was applied along a 50  $\mu\text{m}$  diameter channel yielding a current density of 1018  $\text{A}/\text{m}^2$ . A quantitative comparison of these results with analytical values is presented in Table 1b. The computational time was 110 s, for a simulated physical time of 1000 s.

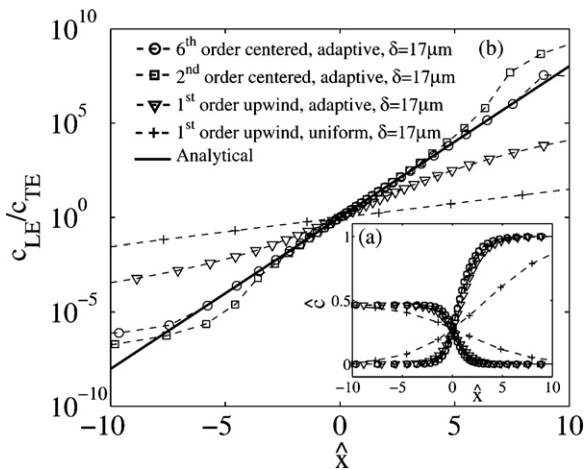


**Fig. 4.** Comparison of the accuracy of various spatial discretization schemes versus an analytical solution (solid line) which yields the shape of an ITP interface. The same constant current is applied in all cases. (a) Non-dimensional concentrations show significant differences in the predicted curves in linear coordinates. (b) The ratio of concentrations is compared with the analytical solution by Saville and Palusinski [4] (log-linear coordinates). The first order upwind schemes deviate significantly from the analytical solution both on a uniform grid and an adaptive grid. The second order centered scheme, being non-dissipative, accurately predicts the slope close to the origin. The higher resolution of the sixth order scheme allows the numerical solution to follow the analytical curve further away from the origin, where the grid size increases significantly.

The sixth order compact scheme (with adaptive grid) is, due to its higher resolution, able to follow accurately the analytical solution significantly further from the origin.

A closer look into the performance of the sixth order compact scheme is provided in Fig. 5, comparing the results obtained for current densities of 0.1, 1, and 5  $\mu\text{A}$  resulting in interface widths ( $\delta$  values) of 175, 17, and 3.5  $\mu\text{m}$  respectively. Fig. 5a presents the concentration profiles in the same non-dimensional scales as Fig. 4. As expected, the results for all three current densities collapse to the same curve. Fig. 5b presents on a logarithmic scale the ratio of LE to TE concentrations versus the normalized axial coordinate. Again, the analytical result (47) appears as a solid line, and over a finite region all three solutions collapse to the same curve. However,

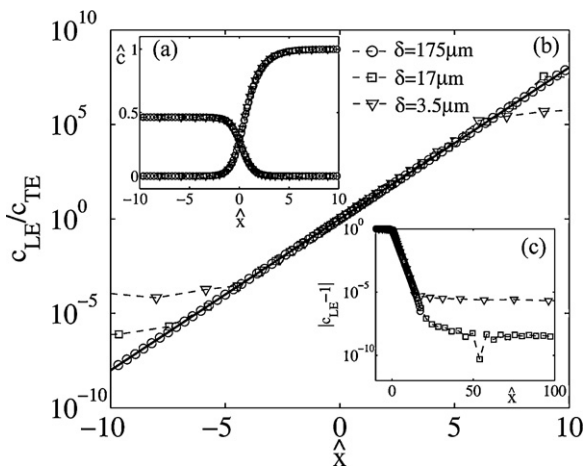


**Fig. 5.** Verification of the high-resolution adaptive-grid scheme in predicting the shape of an ITP interface. (a) Non-dimensionalizing concentration and space collapses the profiles into a single curve. (b) The ratio of concentrations is compared with the analytical solution by Saville and Palusinski [4]. The slope of LE-to-TE concentration ratio is captured precisely at the interface in all three cases, but deviation occurs earlier as current is increased. (c) The error in prediction of absolute LE concentration values far from the ITP interface (large  $\hat{x}$  values).

the three solutions are not entirely self-similar: Since the physical domain length remains unchanged (10 mm) for all cases, the normalized domain length is significantly larger for higher currents. For this reason, the grid spacing away from the interface appears to be larger for higher currents. We intentionally present a slightly under-resolved case (using 100 grid points) in order to note that while the solution accurately captures the interface, it is not free of oscillations. As current increases, the cell Peclet number away from the interface increases, and this ultimately leads to some oscillations. These oscillations can be avoided by decreasing the domain size or by increasing the number of grid points.

We note that although the deviation appears to be significant away from the origin (approximately two orders of magnitude at  $\hat{x} = 10$ ), this is the result of the TE concentration reaching (nearly) zero and thus amplifying the error in the ratio  $c_{LE}/c_{TE}$ . A more direct estimate of the accuracy far from the origin can be obtained by inspecting the deviation of the LE concentration from its plateau value, as presented in Fig. 5c. For the sharpest gradient ( $\delta = 3.5 \mu\text{m}$ ) the error is on the order of  $10^{-6}$ . The error for  $\delta = 17 \mu\text{m}$  is on the order of  $10^{-9}$ . For the widest interface ( $\delta = 175 \mu\text{m}$ ), the finite domain truncates the asymptotic decay of the error before reaching a constant value.

## 5. Results and discussion

### 5.1. Resolution and computational cost

In [8], we provided a comparison of the computational time using a uniform versus adaptive grid for the case of a single ITP interface. To compare solutions with equivalent resolution, we used the minimum grid spacing of the adaptive grid solution in the uniform grid case and used the sixth order compact scheme for both. As expected, the adaptive grid was shown to be more effective as the width of the ITP interface compared with the channel length decreased. For a (typical) 1/1000 ratio (e.g., 20  $\mu\text{m}$  interface in a 20 mm long channel), a 75-fold decrease in the computational time was obtained. For a 1/100 ratio, the computational time decreased only by 5-fold.

However, in addition to the reduction in computational time provided by the adaptive grid, we should compare also the (as we shall see, slightly increased) computational cost associated with the sixth order compact scheme, versus that of a second order centered scheme. Two main factors should be taken into account: First, as discussed in Section 3, the inherent increased resolution of the compact scheme allows it to achieve equal numerical resolution given a decreased number of grid points. This tends to reduce the overall computational cost. Second, the sixth order compact scheme requires an additional solution of a tridiagonal system, which tends to increase computational cost. As discussed in [22], for a fixed spatial resolution, the stable time step remains unchanged and therefore is not considered in this analysis.

We begin by numerically evaluating the reduction in the number of grid points enabled by use of the sixth order compact scheme, while maintaining the same spatial resolution. To remove the coupling between the solution and the behavior of the adaptive grid, which may slightly vary depending on the scheme used, we here disable the adaptive grid mechanism and perform the computations on a uniform grid. The single interface ITP problem presented in Section 4.2 is used here again (with the same species and concentrations). A series of computations using an increasing number of grid points is performed with a fixed current density of 0.5  $\mu\text{A}$ . For each computation, the magnitude of oscillations is monitored; naturally, lower grid density results in higher non-dimensional wave numbers. If these wave numbers are dispersed by the numerical scheme, oscillations will appear. To quantify these oscillations we

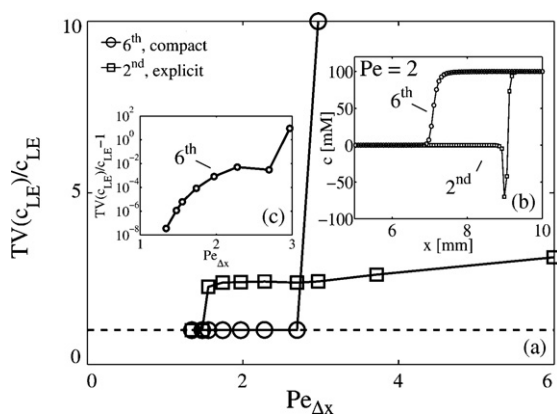


**Fig. 6.** Comparison of the level of oscillation for the sixth order compact scheme and second order explicit scheme. (a) The normalized total variation of the LE concentration versus the cell Peclet number showing that significant oscillations appear earlier (for lower Peclet numbers) for the second order scheme. (b) LE concentration profiles for both scheme demonstrating the oscillation levels for  $Pe_{\Delta x} = 2$ . (c) The residual oscillation of the sixth order scheme on a logarithmic scale, showing some oscillation exist in all presented Peclet numbers, yet decay exponentially.

use the total variation (TV) [32] of the concentration profiles,

$$TV(c) = \sum_{j=2}^N |c_j - c_{j-1}|, \quad (49)$$

where index  $j$  indicates the grid point number, and  $N$  is the total number of grid points in the domain. Since the LE profile should vary monotonically from zero to  $c_{LE}^0$ , the theoretical value of the ratio of  $TV(c_{LE})$  to its maximum concentration  $c_{LE}^0$  is exactly 1. Any oscillations in the concentration profile would increase this value. Fig. 6a presents the value of  $TV(c_{LE})/c_{LE}^0$  as a function of Peclet number, for both the sixth order compact and second order centered schemes after 100 s of simulation time. To illustrate the type of oscillations typically observed, Fig. 6b presents the concentration profile of the LE for both schemes for  $Pe_{\Delta x} = 2$ . At this Peclet number, the sixth order compact scheme is able to resolve the gradient, while the second order centered scheme exhibits oscillations, which result in high values of TV. The Peclet number is based here on the (uniform) grid spacing, the mobility and diffusivity of the LE, and the electric field in the TE region (since the electric field there is higher). For large grid spacing, both schemes show significant oscillations which are on the order of the LE concentration  $c_{LE}^0$ . The main difference between the schemes is in the value of the largest grid spacing for which these oscillations become acceptably small. As shown in the figure, for both schemes this change is rather abrupt, i.e., there exists a threshold value for which the oscillations sharply decay. However, the sixth order scheme allows much larger grid spacing to be used, and the ratio of Peclet numbers for which the parameter approaches 1, within a tolerance of  $10^{-2}$ , is approximately 1.8. We note that while the oscillation significantly decay for Peclet numbers smaller than the threshold, the solution is not entirely oscillation free but rather oscillates at much smaller amplitudes. Fig. 6c presents on a logarithmic scale the decay in the total variance parameters as Peclet number is decreased. In summary, due to its higher resolution the sixth order compact scheme allows for approximately a 1.8-fold decrease in number of grid points, while maintaining the same resolution.

Next, we performed a separate set of numerical simulations to evaluate the additional computational cost associated with solving a tridiagonal system for every spatial derivative computed using the sixth order compact scheme. However, since the computation of derivatives comprises only part the total computation effort within each time step (equilibrium chemistry solution, adaptive

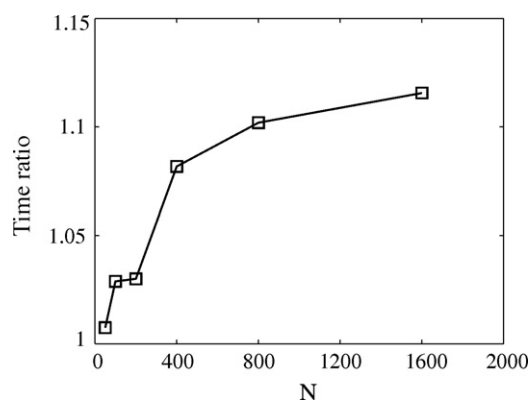


**Fig. 7.** The ratio between the time required for the sixth order compact scheme to calculate the flux derivatives (right-hand side of Eq. (8)) to the time required for the second order centered scheme to perform the same operation. For larger grids, the relative weight of the overhead in the calculation becomes smaller and the curve asymptotes to a constant value.

grid cost function calculation, and boundary conditions enforcement are some of the other computations routinely performed), it is important to evaluate this additional cost in the setting of a realistic ITP problem. We therefore consider here again the case of a single ITP interface, but with the adaptive grid and chemical equilibrium operating. 100 mM hydrochloric acid, 20 mM acetic acid, and 150 mM TRIS were used as LE, TE and counter-ion respectively. A low current of  $0.1 \mu\text{A}$  on a  $50 \mu\text{m}$  diameter channel was used in order to avoid oscillations. Using a large number of time steps (at least several thousands per case), the time per computation of flux derivatives (right-hand side of (8)) was evaluated. This was performed for both the sixth order compact and the second order centered schemes. Fig. 7 presents the computational time ratio obtained as a function of the grid size. The increase in the time ratio as the number of grid points increases suggests the existence of an approximately constant overhead operation whose relative weight becomes smaller. The current implementation was programmed in Matlab (The Mathworks<sup>TM</sup>, Natick, Massachusetts, USA), and it may be that an implementation in a compiled form would yield a smaller overhead and a more uniform time ratio. To make a conservative estimate, we may consider the highest time ratio obtained as representative. This result then shows that for the same number of grid points, the second order centered scheme is approximately 12% faster than the sixth order compact scheme.

In summary, the gain from the additional resolution of the sixth order compact scheme (which allows for a reduction in the number of grid points) is therefore greater than the loss due to the solution of the additional tridiagonal system. However, exact values for this benefit likely depend on the existence of other physical modules in the simulation, on the programming language used and on the overall quality of the implementation. For the current implementation, using the two aforementioned numerical tests, we estimate the sixth order compact scheme to be approximately 60% faster than the second order centered scheme, for the same final resolution.

## 5.2. Adaptive grid and boundary conditions

Here, we illustrate the performance of our adaptive grid and boundary condition formulation on a physically relevant ITP problem. Consider ITP focusing (from low initial concentration) of the anion Arsenic acid. Table 2 lists chemical properties and initial concentration of various electrolytes used in this system. A current density of  $500 \text{ A/m}^2$  was considered in a 10 mm long domain (equivalent to  $1 \mu\text{A}$  through a  $50 \mu\text{m}$  diameter capillary). We apply a uniform counter-flow equal in magnitude to the electrophoretic

**Table 2**  
Equilibrium constants, corresponding valences, fully ionized electrophoretic mobilities (at negligible ionic strength), and initial concentrations for the electrolytes used in the simulation of Section 5.2. Chemical properties are obtained from Hirokawa et al. [33].

Name	$pK_a$	Valences	Mobility ( $\times 10^{-9} \text{ m}^2 \text{ V}^{-1} \text{ s}^{-1}$ )	Diffusivity ( $\times 10^{-10} \text{ m}^2/\text{s}$ )	Initial concentration
Hydrochloric acid (LE)	-2	-1, 0	-79.1	20.3	20 mM
Acetic acid (TE)	4.756	-1, 0	-42.2	10.8	8 mM
TRIS (counter-ion)	8.076	0, +1	29.5	7.6	30 mM
Arsenic acid (ACE)	6.94, 2.19	-2, -1, 0	-70.0, -3.52	9.0	10 $\mu\text{M}$

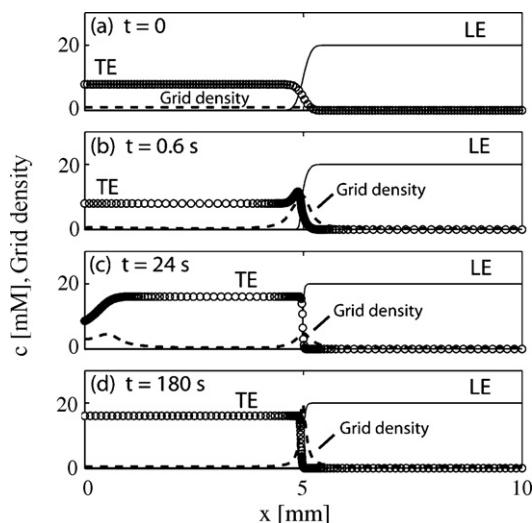


**Fig. 8.** Simulation showing distributions of LE and TE ions (solid curve) in an ITP focusing of arsenic acid in a 10 mm long domain using 150 grid points. Superposed is a plot of grid density (dashed curve). The circles on the TE curve indicate the location of grid point and show the clustering of grid points in regions of high concentration. The case is solved in a frame of reference moving with the zone, with hydrochloric acid as LE, acetic acid as TE, and TRIS as a counter-ion ( $\text{pH} \sim 7.8$ ). (a) The initial conditions consist of a diffused interface between the LE and TE on a uniform grid (grid density equals 1.0 everywhere). (b) Immediately after electromigration begins, the LE-TE interface sharpens and local grid density increases. (c) The TE concentration adjusts to a new value, and a TE concentration interface is swept towards the TE reservoir. A slight increase in grid density follows this high-gradient TE interface as it propagates leftward. (d) The high-gradient TE interface has now passed through the left boundary and most grid points now migrate towards the LE-TE interface, increasing local grid density. The computational time was 585 s for the total simulated physical time of 180 s.

velocity of the LE, so that sample zone is conveniently stationary (and so a solution in a frame of reference moving with the sample zone is obtained). The computational constants used for this case are  $\lambda = 5$  and  $N_l = 10$ . Fig. 8 presents a sequence of images corresponding to various times in the focusing process. Initially, the TE concentration at the interface increases due to a large influx (from the left) and zero outflux (TE ions cannot overtake LE ions). The adaptive grid responds to the local increase in gradients by increasing local grid density. When the TE concentration reaches its Kohlrausch value [23], the region of increased TE concentration migrates towards the left-hand reservoir until the entire TE adjusts to a new concentration.

Note that while TE ions electromigrate towards the right, this concentration wave moves towards the left. This is due to the fact that the electric field is strongly coupled to the TE concentration, and is higher where the concentration is lower. The overall ion flux is higher in region of low concentration, and this causes a local increase in concentration. As shown in Fig. 8c, an increased grid density follows this wave up to the left boundary. The wave smoothly passes through the boundary and leaves the TE at a uniform concentration. The latter phenomenon is an example where ion velocity direction alone insufficiently describes the propagation of concentration waves (see Section 3.4 regarding boundary conditions). Next, the grid points automatically redistribute and

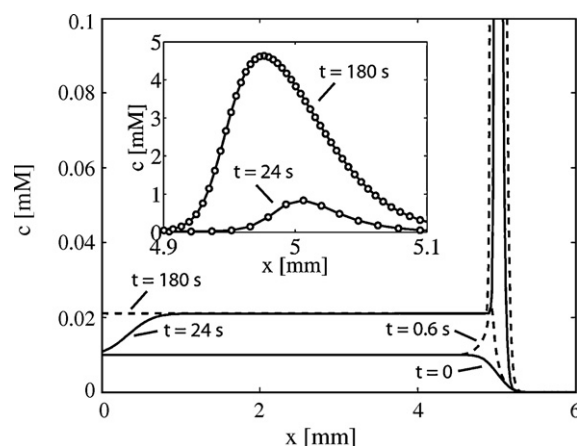


**Fig. 9.** Simulation showing the ITP focusing of arsenic acid for the same case presented in Fig. 8. The initial concentration of the analyte is 10  $\mu\text{M}$ , and it is initially present only in the TE portion of the domain (corresponding to a semi-infinite sample case where sample is loaded with the TE into the TE reservoir). Upon application of an electric field, the analyte starts to focus at the interface between the LE and TE ( $t = 0.6 \text{ s}$ ). The TE concentration adjusts to a new value as it migrates into the region formerly occupied by LE; and this adaptation is accompanied by a decrease in the electric field. The latter adjustment in turn increases the concentration of the analyte throughout the channel ( $t = 24 \text{ s}$ ). At  $t = 180 \text{ s}$ , the adaptation is complete, the gradient in the TE has migrated out of the left boundary, and the left portion of the channel has obtained a new concentration. The inset shows the concentration profiles of the sample at  $t = 24 \text{ s}$ , 180 s on a larger y-axis scale, with circles indicating the location of grid points. The sample zone is still in peak mode and sample peak concentration continues to increase. Note that the maximum sample concentration has increased by more than two orders of magnitude.

more of them now migrate towards the high gradient regions of the interface.

Fig. 9 shows the behavior of the focusing analyte for the same simulation times presented in Fig. 8. The initial distribution of the

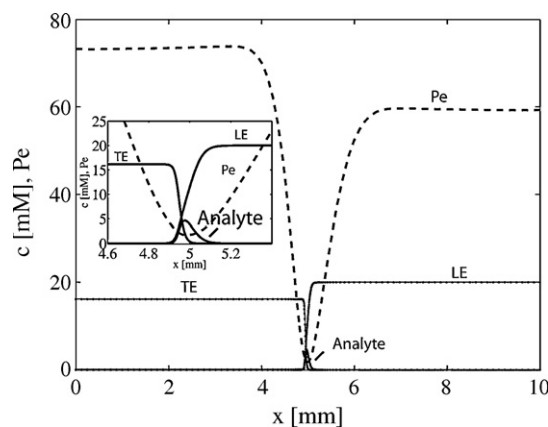


**Fig. 10.** The distribution of cell Peclet number,  $Pe = a \Delta x/D$ , throughout the domain for the case presented in Fig. 8 at time  $t = 180 \text{ s}$ . As shown in the inset, the Peclet number near the interface decreases significantly to allow a non-oscillatory solution. Far from the interface, where concentration gradients vanish, the Peclet number increases by roughly two orders of magnitude. Yet these regions are also free of (dispersion based) oscillation as the physical wave numbers in those regions are small.

analyte represents a semi-infinite sample which is mixed homogeneously with the TE (it is semi-infinite as there is no limit to the number of analyte molecules which can arrive from the left-hand reservoir). The analyte's concentration at the interface increases continuously, reaching nearly a 500-fold increase after 180 s. In this example, the analyte's initial concentration is approximately three orders of magnitude lower than that of the buffer, so it has negligible effect on the local electric field (sample is in peak mode). The adaptation of the TE to new concentration values is accompanied by a decrease in the electric field, which in turn increases the concentration of the analyte throughout the channel. The analyte's concentration front follows that of the TE and propagates towards the TE well, eventually crossing through the left-hand boundary. Fig. 10 presents the maximum cell Peclet number throughout the channel at  $t = 180$  s. As expected, most of the domain experiences Peclet numbers which are much larger than the aforementioned restrictive requirement of (10) proposed in 1991 by Dose and Guiochon [4], and yet we obtain a non-oscillatory solution. Only within the high-gradient interface region does the Peclet number reduce to satisfy this requirement.

## 6. Conclusions

We developed an efficient numerical solver which is able to accurately resolve sharp ITP interfaces while reducing the computational cost. This was achieved by utilizing a sixth order compact scheme coupled to an adaptive grid which focuses grid points within regions of interest. The adaptive grid we developed uses a unique variational approach in which a grid mapping function (from a non-uniformly spaced physical domain to a uniformly spaced computational domain) is marched in time so to minimize gradients in the computational domain. This approach was found to be especially suitable for ITP problems where one or more narrow, high gradient regions migrate within long domains which otherwise contain low or even zero gradients. To facilitate simulations performed in a frame of reference moving with the ITP zones (allowing reduction in the domain size), we developed a set of characteristics based boundary conditions. These boundary conditions account for the strong coupling between the different species and allow, under several assumptions, for concentration waves to freely cross the boundaries.

Finally, extensive verification of the method was performed by comparing both plateau values and interface shapes with available analytical solutions. Further numerical tests demonstrated the increased resolution obtained by the use of the sixth order compact scheme. These tests showed that the penalty in computational cost associated with the compact scheme is small compared with the gain in cost due to the reduction in the number of grid points (enabled by its increased resolution). Most of the computational gain remains however due to the adaptive grid, reducing the computational time by one to two orders of magnitudes for realistic isotachopheresis problems.

Overall, the computational approach presented allows practitioners to obtain fast and accurate predictions of ITP assays on a

personal computer and sets the ground for possible optimizations or inverse problems using a fast solver as their core.

## Acknowledgements

M.B. is supported by an Office of Technology Licensing Stanford Graduate Fellowship and a Fulbright Fellowship. The authors thank William R. Wolf from the Department of Aeronautics and Astronautics at Stanford University for insightful discussions and constructive comments. We gratefully acknowledge support from the Micro/Nano Fluidics Fundamentals Focus (MF3) Center funded by Defense Advanced Research Projects Agency (DARPA) MTO Grant No. HR0011-06-1-0050 and contributions from MF3 corporate members.

## Appendix A. Supplementary data

Supplementary data associated with this article can be found, in the online version, at doi:10.1016/j.chroma.2009.11.072.

## References

- [1] P.A. Auroux, D. Iossifidis, D.R. Reyes, A. Manz, *Anal. Chem.* 74 (2002) 2637.
- [2] P.S. Dittrich, K. Tachikawa, A. Manz, *Anal. Chem.* 78 (2006) 3887.
- [3] L. Chen, J.E. Prest, P.R. Fielden, N.J. Goddard, A. Manz, P.J.R. Day, *Lab Chip* 6 (2006) 474.
- [4] R.A. Mosher, D. Dewey, W. Thormann, D.A. Saville, M. Bier, *Anal. Chem.* 61 (1989) 362.
- [5] R.A. Mosher, C.X. Zhang, J. Caslavská, W. Thormann, *J. Chromatogr. A* 716 (1995) 17.
- [6] W. Thormann, C.X. Zhang, J. Caslavská, P. Gebauer, R.A. Mosher, *Anal. Chem.* 70 (1998) 549.
- [7] V. Hruska, M. Jaros, B. Gas, *Electrophoresis* 27 (2006) 984.
- [8] M. Bercovici, S.K. Lele, J.G. Santiago, *J. Chromatogr. A* 1216 (2009) 1008.
- [9] E.V. Dose, G.A. Guiochon, *Anal. Chem.* 63 (1991) 1063.
- [10] M.C. Breadmore, R.A. Mosher, W. Thormann, *Anal. Chem.* 78 (2006) 538.
- [11] T.L. Sounart, J.C. Baygents, *J. Chromatogr. A* 890 (2000) 321.
- [12] S.V. Ermakov, M.S. Bello, P.G. Righetti, *J. Chromatogr. A* 661 (1994) 265.
- [13] J.H.P.A. Martens, J.C. Reijenga, J.H.M.T.T. Boonkcamp, R.M.M. Mattheij, F.M. Everaerts, *J. Chromatogr. A* 772 (1997) 49.
- [14] N. Ikuta, T. Hirokawa, *J. Chromatogr. A* 802 (1998) 49.
- [15] J.W. Yu, Y. Chou, R.J. Yang, *Electrophoresis* 29 (2008) 1048.
- [16] M. Bier, O.A. Palusinski, R.A. Mosher, D.A. Saville, *Science* 219 (1983) 1281.
- [17] D.A. Saville, O.A. Palusinski, *AIChE J.* 32 (1986) 207.
- [18] M. Stedry, M. Jaros, V. Hruska, B. Gas, *Electrophoresis* 25 (2004) 3071.
- [19] O.A. Palusinski, A. Graham, R.A. Mosher, M. Bier, D.A. Saville, *AIChE J.* 32 (1986) 215.
- [20] W.F. Spatz, G.F. Carey, *Int. J. Numer. Methods Heat Fluid Flow* 8 (1998) 288.
- [21] A. Jameson, L. Martinelli, J.J. Alonso, J.C. Vassberg, J. Reuther, *Aerosp. Conf. Proc.*, vol. 2, 2000, p. 55.
- [22] S.K. Lele, *J. Comput. Phys.* 103 (1992) 16.
- [23] F. Kohlrusch, *Ann. Phys.* 298 (1897) 209.
- [24] T.M. Jovin, *Biochemistry* 12 (1973) 871.
- [25] R.A. Alberty, *J. Am. Chem. Soc.* 72 (1950) 2361.
- [26] G.T. Moore, *J. Chromatogr.* 106 (1975) 1.
- [27] A.M. Enlund, S. Schmidt, D. Westerlund, *Electrophoresis* 19 (1998) 707.
- [28] T.K. Khurana, J.G. Santiago, *Anal. Chem.* 80 (2008) 6300.
- [29] F.M. Everaerts, J.L. Beckers, T.P.E.M. Verheggen, *Isotachopheresis: Theory, Instrumentation, and Applications*, Elsevier, Amsterdam, 1976.
- [30] O.A. Palusinski, Y. Su, P.C. Fife, *Electrophoresis* 11 (1990) 903.
- [31] D.A. MacInnes, L.G. Longworth, *Chem. Rev.* 11 (1932) 171.
- [32] A. Harten, *J. Comput. Phys.* 49 (1983) 357.
- [33] T. Hirokawa, M. Nishino, Y. Kiso, *J. Chromatogr.* 252 (1982) 49.